Chapter 3

Evolution of Edge-On Oriented Polymer Films Self-Assembled at the Air–Liquid Interface for High-Performance Electronic Device Applications

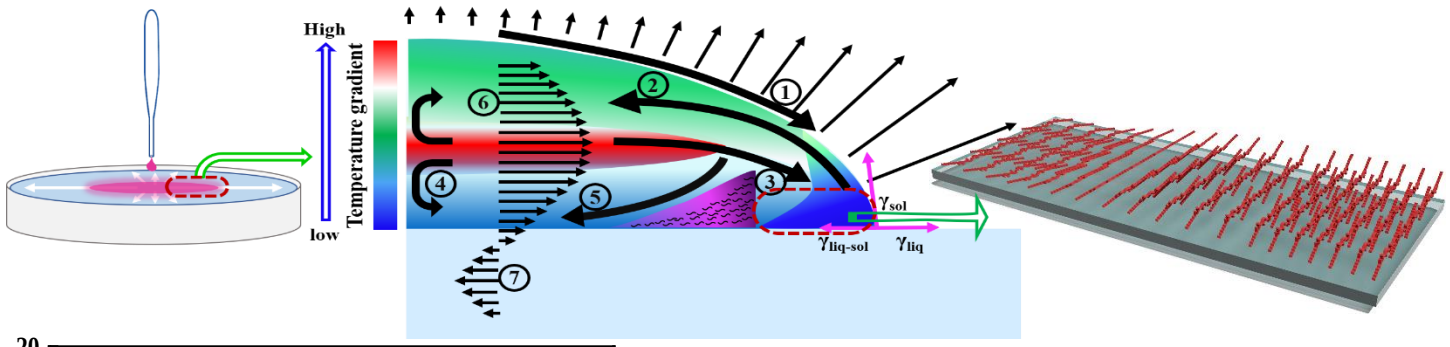

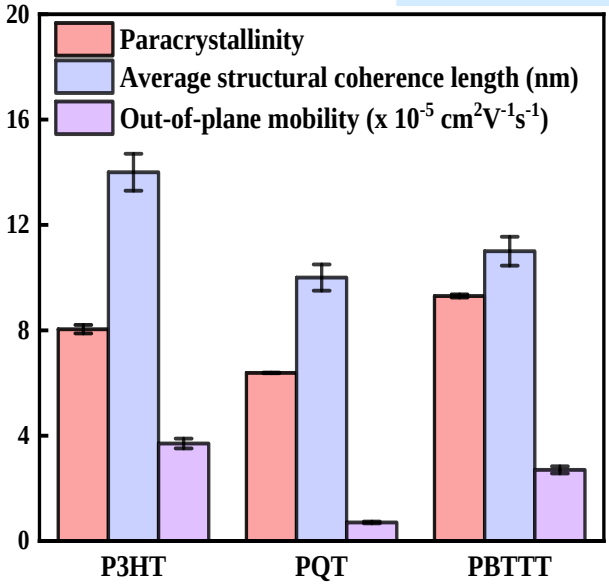

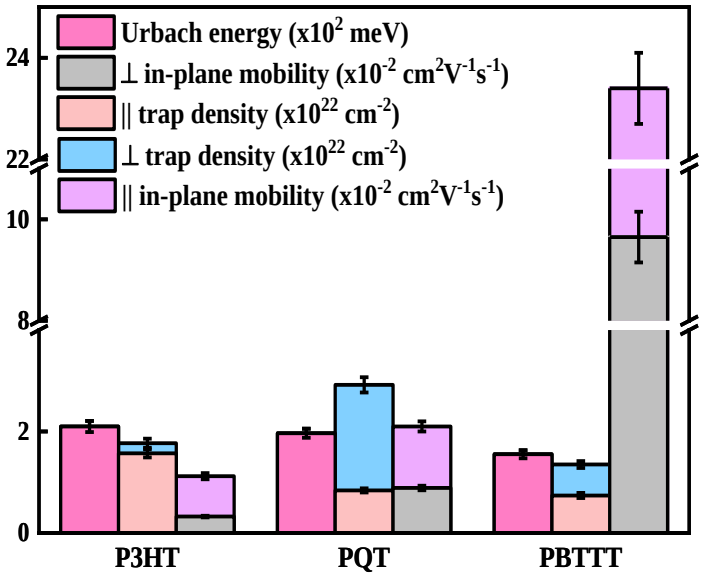

3.1.Introduction

The performance and operational lifetime of organic semiconducting material-based electronic and optoelectronic devices depend on the degree of electron delocalization through molecular orbital overlap between adjacent molecules [82]. Defects, which are susceptible to organic semiconductors because of weak Van der Waal interactions, disrupt significantly the molecular wavefunction overlap [83,84]. Thus, it is crucial to understand and control the interplay between microstructural complexity and charge transport properties for developing high-performance organic electronic devices. One of the most effective way-outs known to enhance carrier mobility is the uniaxial orientation of these quasi-one-dimensional OSPs. Although many innovative thin-film technologies have been developed for this purpose, [57] they still lack industrial-level scalability, performance and an operational lifetime to compete with their inorganic counterpart. Therefore, a deposition technique is needed to precisely control the polymer chain ordering and crystalline orientation of semiconductor domains.

Polymer self-assembly at air-liquid interface, also known as 'Floating-film Transfer Method' (FTM), [57] proved to be much more advantageous in terms of ease of film fabrication and the lengthscale up to which molecules are uniaxially oriented. FTM can precisely control the polymer chain ordering and crystalline orientation of semiconductor domains and minimize significant production costs by reducing material waste up to ~95%, as discussed in the experimental section. Although FTM yields highly anisotropic polymer chain stacking at the macroscopic level, during convective Marangoni spreading of polymer solution and solidifying from lyotropic liquid crystal state to solid polymeric films, many cumulative and non-cumulative disorders are associated with the polymeric semicrystals [84–86]. A high degree of conformational freedom often leads to disorders like chain folding, backbone twisting, and tilting, which causes the coexistence of

amorphous region as well as highly ordered domains in OSPs [87]. While these amorphous regions are mostly assumed to introduce electronic trap states, static statistical fluctuation within the microcrystalline domain can also significantly affect carrier mobility [83,88].

To study the charge transport mechanism through localized and delocalized electronic states, we have chosen three different polymer backbone structures (P3HT, PQT, and PBTTT) among the widely studied thiophene family, having different solubility, backbone rigidity, and side-chain length and density. The chemical inconsistency between nonpolar side chains and polar π-conjugated backbone creates a well-defined local phase separation. Thus, all three polymer films show progressive evenly spaced diffraction peaks at low angles along the side chain stacking direction. Now, the presence of lattice disorder as well as non-uniform solvent evaporation at the grain boundaries results in non-uniform strain, which causes lattice parameter fluctuation ($e_{r.m.s.}$) from one diffracting volume to another and paracrystalline disorder (g) [83,89]. Paracrystallinity, first pioneered by Hosmann, is defined as the mean statistical fluctuation of individual lattice spacing, which usually varies from 0-15% [90].

This work investigates the degree of paracrystallinity along the direction of side-chain interdigitation using the diffraction line-shape analysis technique developed by Warren-Averbach (W-A) [91]. Whereas the presence of lattice bending and lattice parameter fluctuation along the π-π stacking direction within crystalline domains is directly visualized from the bright field HR-TEM (high resolution-transmission electron microscope) images. Paracrystallinity introduces an exponential tail of localized wavefunctions from the band of delocalized states into the bandgap, which significantly affects the intermolecular charge transfer integrals. In this study, we have calculated the Urbach tail width similar to inorganic crystals [92,93] for all three polymer films from the UV-Vis absorption spectra. After that, we measure the out-of-plane and in-plane charge carrier mobility for these

polymers using Schottky barrier diode (SBD) and field-effect transistor (FET) structure in bottom-gate top contact (BGTC) mode. We also explored the local electrical anisotropy by measuring the field-effect mobility with channel parallel and perpendicular to the in-plane molecular orientation. Thus, quantifying the paracrystalline disorder, Urbach tail width, exciton-phonon coupling, along with charge transport properties in all three directions, helps us picture the fundamentals of structure-property correlation. Moreover, we have proposed a model mechanism of polymeric thin-film growth at the air-liquid interface, which will help us comprehend and tune the self-assembly in pursuit of engineering and designing high-performing organic electronic devices by further optimizing the processing conditions.

3.2.Results and Discussion

3.2.1. Film growth mechanism:

Regioregular grafting of alkyl side-chain helps these thiophene derivatives to go for self-assembly, minimizing steric hindrance during thin film formation. Polymer crystal growth in films floating on a liquid subphase is being controlled by several parameters like solubility of polymers in nonpolar solvent, the surface free energy of the solvent, relative thermal conductivity, relative viscosity, temperature gradient, density fluctuation, spreading co-efficient and evaporation flux. After removing all the thermal history, the low surface energy polymer solution was dropped over a high surface energy hydrophilic liquid mixture. The spreading of polymeric solution over the hydrophilic liquid bed due to tangential stress caused by interfacial surface tension gradient is basically a low Renolds no flow. As we are spreading a microscopically disentangled and relatively low concentration (10 mg/ml) polymer solution which behaves like a Newtonian fluid, [94] lubrication theory and steady-state Navier-Stokes equations can be used to solve the velocity profile (which is parabolic in nature) of the thin-film flow [95,96]. As shown in

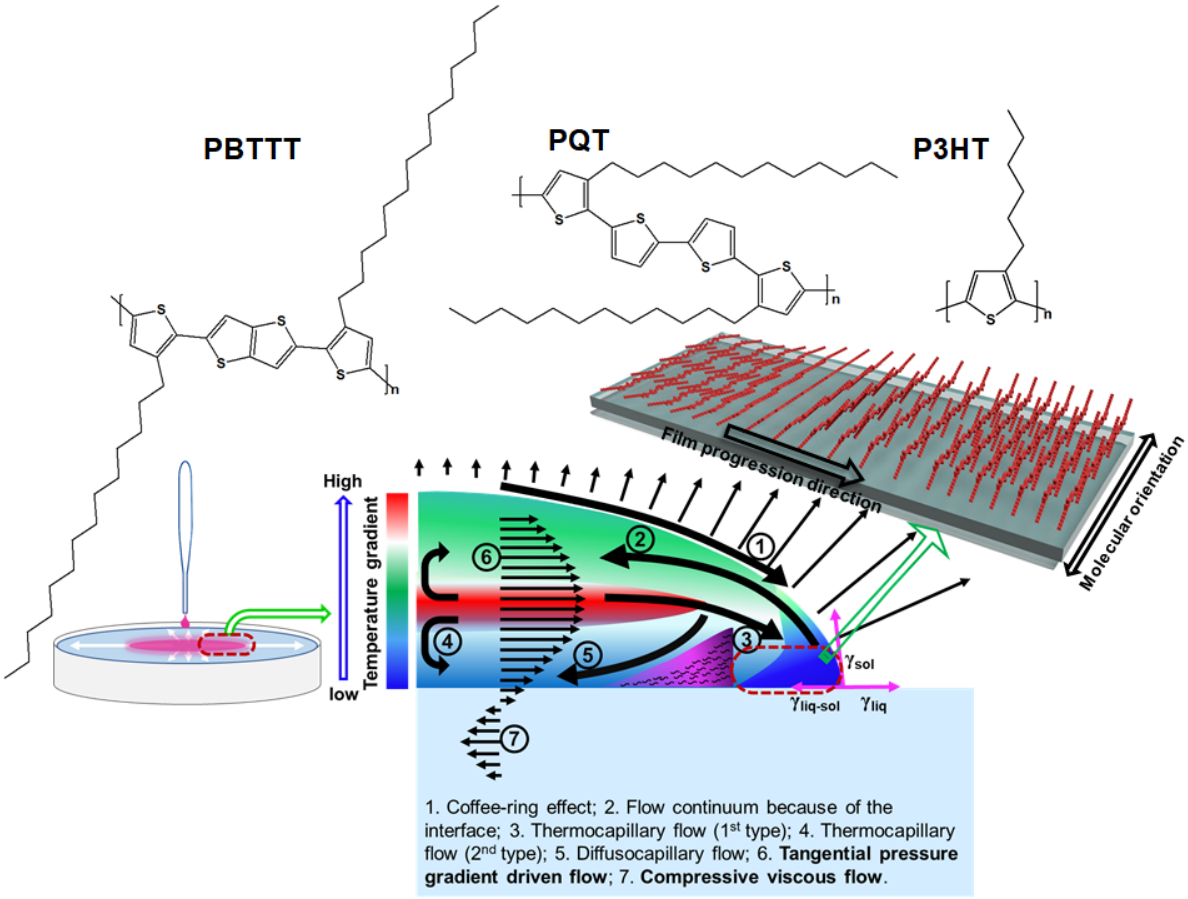

Figure 3.1 Schematic representation of three model polymers with their self-assembly and film formation mechanism at air-liquid interface.

the Figure 3.1, during spreading, the solvent evaporates in a "stick-slide" mode, [97] where some portion of the solution sticks at the liquid-liquid interface due to dipole-dipole interaction between chloroform and Glycerol; the rest of it slides with continuous depinning of the triple contact line (air-liquid-liquid). Since diffusion-limited evaporative flux is highest (theoretically infinite) at the contact line because of the highest surface to volume ratio, [97] the free surface squeezes the solution outward towards the edge of the progressing film (flow 1), also known as the coffee-ring effect [98]. Moreover, while endothermic divergent mass flux creates a temperature gradient causing a thermocapillary flow depositing solute towards the edge (flow 3). As these two flows remove mass from the inside and face a constraint at the air-solution interface, a reverse flow exists to maintain

the flow continuity (flow 2), which is less intense. At the same time, the surface concentration gradient creates a diffusocapillary flow towards the apex (flow 5) [98]. Now, the thermal conductivity of air is significantly less than the bottom liquid substrate, which originates a temperature gradient between the air-solution and the liquid-solution interface, causing solutal deposition at the center (flow 4) [99]. Finally, the pressure gradient along the interface is much superior than along the height because of the thickness of the film (~nm) is much less than its length (~cm). Consequently, the tangential stress (flow 6) can be poised only by compressive viscous force linked with the polymeric solution flow (flow 7). While the OSP lamellae move along these outward flows (1,3 and 6), they face two resistances: the compressive viscous force working at the solution-liquid interface and the air-solution interface at the boundary. These two resistances are the protagonist to help these fish-bone-like polymeric backbones to self-assemble in an out-of-plane "edge-on" fashion as evidenced in HR-TEM images. This edge-on structure becomes a stable conformation in the dried thin film because of the high evaporation flux present at the end of the progressing film. In this way, we get uniaxial and highly edge-on oriented polymeric thin film by manipulating the relative orientation and spacing between proximate molecules.

Nevertheless, owing to these complex flow patterns during spreading and solidification, many cumulative paracrystalline disorder manifests in the microcrystalline domains. Although all three backbone structures are prone to edge-on conformation in response to the compressive viscous flow and restricting interface, the planar PBTTT skeleton should take more edge-on conformation than allow lattice fluctuation due to rigidity. At the same time, the most flexible P3HT (and PQT also) backbone balances some of the forces by adopting many structural defects.

3.2.2. Thin film characterizations

To study the structure and orientation present inside the polymer film, we have employed the meridional XRD (X-Ray diffraction) scan [i.e., the scattering vector is almost perpendicular to the substrate surface; Figure 3.2 (a, b)] on PAT films. All the three polymer films show progressive diffraction peaks along (*h*00), which is assigned as the 'a'-axis, i.e., along the side-chain interdigitation. The interplanar spacing d_{h00} are found to be 16.68Å, 17.32Å and 21.66Å for P3HT, PQT and PBTTT respectively, which are congruous with theoretical models as well as previous experiments [100,101]. The difference in d-spacing along the a-axis for these three polymers can be attributed to the dissimilarity in side-chain length, degree of interdigitation, and the tilting of polymer backbones across the c-axis. John E. Northrup theoretically evidenced the extent of side-chain interdigitation directly governs the stability of the polymer [101]. According to his theoretical predictions, the lamellar spacing, d_{100} for PBTTT-C14 is 41.6 bohr which is in accordance with our result (40.9 bohr for PBTTT-C14). Microcrystalline lattice disorder which are cumulative in nature, [84,88] usually shows a functional dependency on the order of diffraction (*n*) for a given set of reflections, whereas diffraction peak broadening originating from finite coherence length is independent of '*n*'. Thus, to decouple size broadening and cumulative disorder along (*h*00) direction, we have used the diffraction line-shape analysis technique developed by Warren-Averbach (W-A) after appropriate correction for background and instrumental broadening [91]. According to the W-A approach, the nth order Fourier coefficient for the h-order diffraction peak is expressed as,

$$A_h(n) = A^s(n) \exp\left[-2\pi^2 h^2 (ng^2 + n^2 e_{rms}^2)\right] \qquad (3.1)$$

Where, $A^s(n)$ corresponds to the size-broadening and other parameters discussed earlier in the introduction.

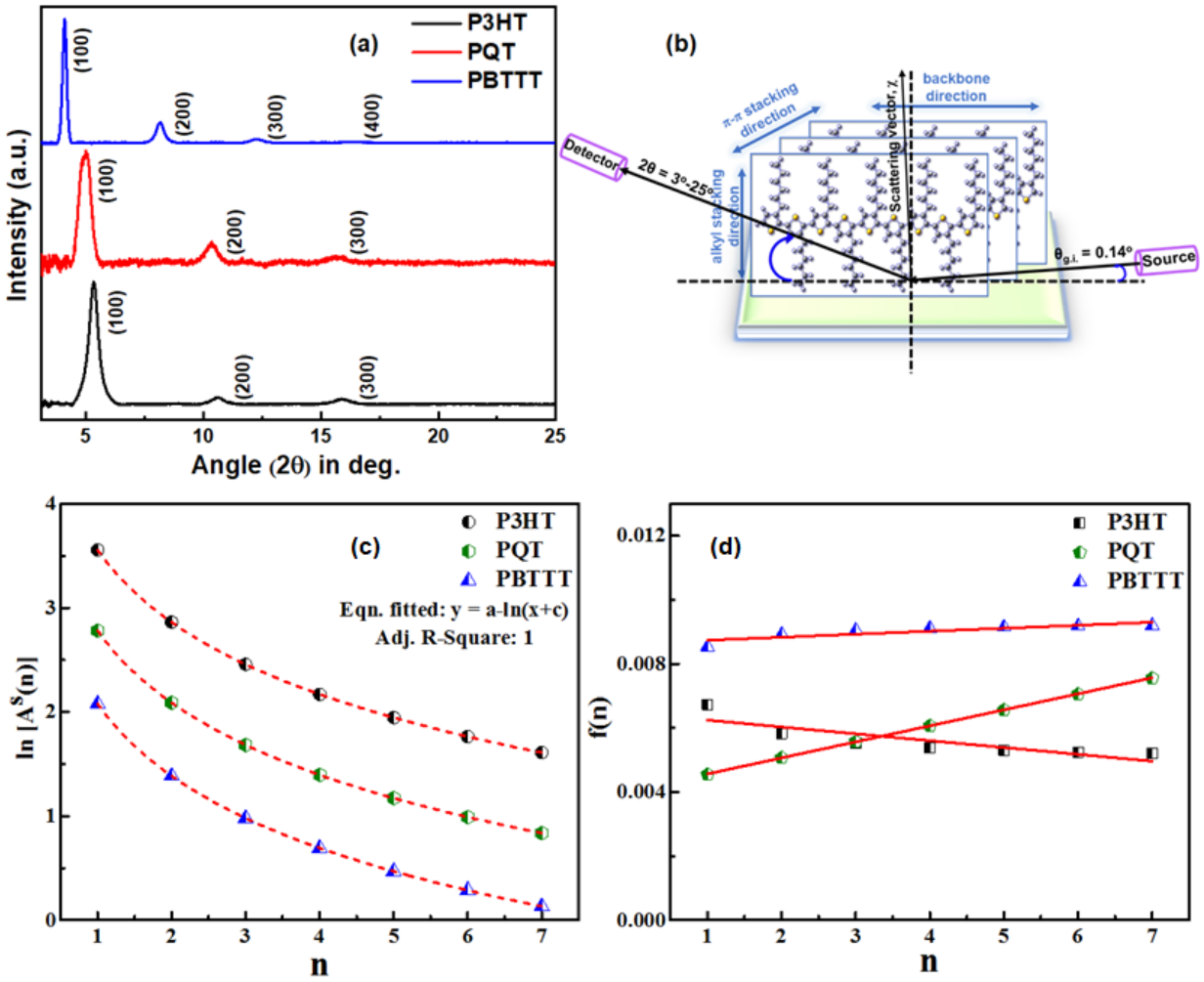

Figure 3.2 (a) Out-of-plane XRD spectra of P3HT, PQT and PBTTT films scanned keeping source fixed at grazing incidence angle 0.14°, (b) schematic of the XRD measurement, (c) $\ln[A^s(n)]$ vs n plot and (d) $f(n)$ vs n plot which yield us the values of M, g^2 and e_{rms}^2.

Table 3.1 Findings of peak shape analysis

Sample	**Average d_{h00} in nm**	**Coherence length along (h00)**		$g(\%)$	$e_{rms}(\%)$
		W-A graphical, M (nm)	**Scherrer, L_c (100) in nm**		
P3HT	1.668	14	16.26	8.04±0.16	1.46±0.19
PQT	1.732	10	14.89	6.38	0.71±0.01
PBTTT	2.166	11	37.67	9.3±0.06	0.97±0.11

Now, taking logarithm, we can rewrite the equation (1) as follows,

$$\ln[A_h(n)] = \ln[A^s(n)] - 2\pi^2 h^2 n f(n) \quad (3.2)$$

Here, $f(n) = g^2 + ne_{rms}^2$; Now, from the $\ln[A_h(n)]$ $vs\ h^2$ plot (Supporting) for different values of n, we can easily decouple the size coefficient (y-intercepts) from the disorder terms (slopes). Thereafter, as shown in Figure 3.2 (c, d), a linear fit of $f(n)$ $vs\ n$ and fitting of $\ln[A^s(n)]$ $vs\ n$ yield us the values of M, g^2 and e_{rms}^2 which are tabulated in Table 3.1. Now, according to Hosmann et al., $g < 1\%$ corresponds to highly ordered crystals, and $1 - 10\%$ represents typical paracrystals and $10 - 15\%$ defines the amorphous [90]. W-A peak shape analysis reveals that degree of paracrystallinity and lattice parameter fluctuation are lowest for PQT (6.38% and 0.71%), while for P3HT and PBTTT it is almost comparable. The side chain density in P3HT is nearly twice that in PQT and PBTTT, which makes its backbone more flexible as compared to others and the most affected polymer due to non-uniform lattice strain (highest e_{rms} value). At the same time, the presence of intrinsic gauche conformation along with a long 14C-alkyl chain packing disorder leads to the highest paracrystallinity for PBTTT along the (h00) direction. The value of average coherence length along the side-chain stacking direction calculated using Scherrer expression (Supporting) is reduced after taking into account the compound effect of cumulative disorder. This disparity in two results is because of firstly, Scherrer formula assumes that only size contributes to the peak broadening neglecting the pervasive lattice disorder and secondly, the presence of high proportion smaller crystallites in the FTM films which introduces gaussian tail in the diffraction peak rather than a proper contribution to the peak broadening [88]. The higher the degree of paracrystallinity in FTM films, the deeper will be the trap states, even the band of the delocalized density of states becomes more localized, and thus more severely it will affect the charge transport.

Thin film XRD probes domains macroscopically in oriented thin films, which scatter coherent radiation, but through HR-TEM we can visualize the 2D-projections of the local in-plane orientation of the polymer chains in crystalline domains. As shown in Figure 3.3 (a-c), all the SAED (selected area electron diffraction) patterns composed of a number of Scherrer rings with different intensities confirm different periodicity of the structure microscopically. Now, the presence of both (0*k*0) and (0*k*1) reflections justifies the coexistence of "face-on" and "edge-on" oriented crystalline lamellae in the film interior. Nonetheless, intense (020) equatorial reflection in all three polymer films evidenced the "edge-on" lamellae population subjugates the local crystal orientation in the film plane [102]. In bright-field (BF) mode, the HR-TEM images [Figure 3.3 (d-f)] show alternating dark and bright stripes in the case of all three polymer films which are originated from different molecular packing according to M. Brinkmann et al. [87] In case of semicrystalline polymers, crystalline regions appear as dark because of ordered chain packing and the amorphous interlamellar zones as bright contain tie chains, chain ends and folds. Marangoni flow-driven orientation and self-assembly of conjugated polymer backbones over liquid subphase is highly susceptible to chain folding. As previously evidenced by M. Brinkmann et al. [87,102] and Grevin et al., [103] chain folding is one of the fingerprints of all classical semicrystalline polymers. In our work, polymer chain folding and tilting are clearly noticeable in the bright field HR-TEM images. The folding of conjugated polymer chains, i.e., lattice bending, is the consequence of impurities, amorphous interlamellar domains and lattice-strains produced by solvent evaporation at grain boundary [84]. As the HR-TEM images project "edge-on" oriented lamellae, the edge of the crystalline domains, i.e., domain boundaries, correspond to the fold surfaces. These

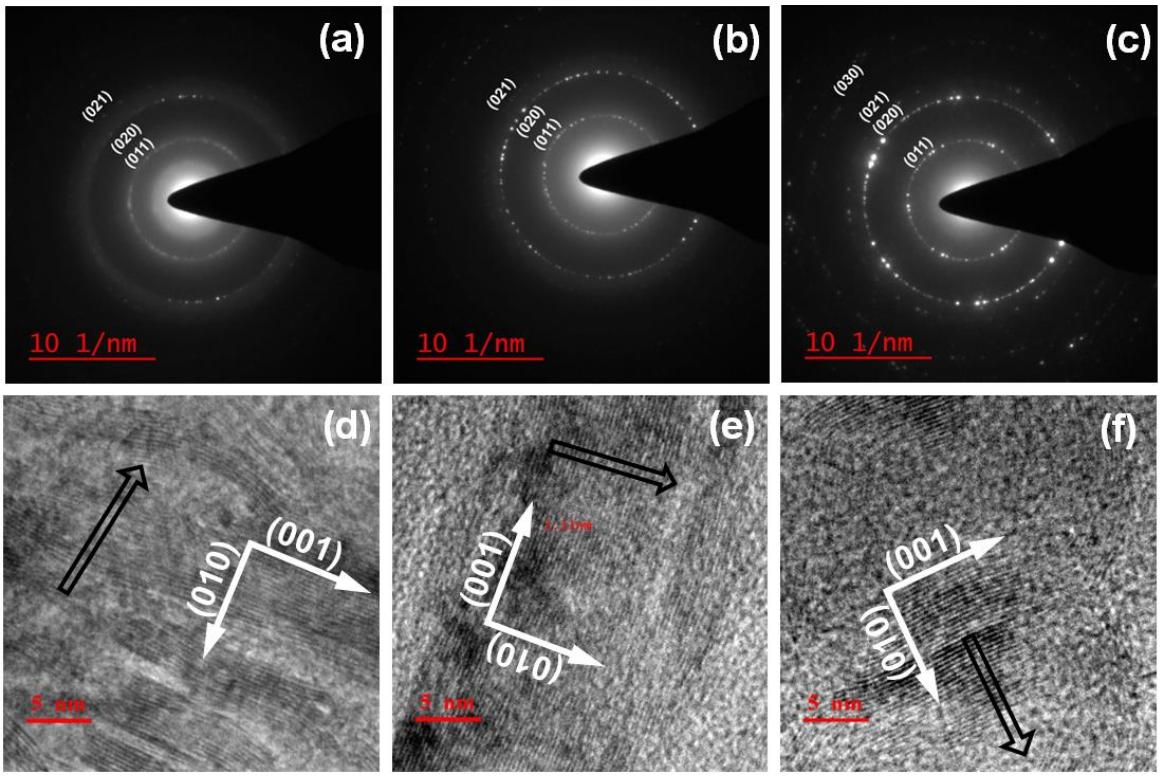

Figure 3.3 (a-c) SAED patterns of the oriented thin films (≈ 15±2 nm thick) of PBTTT, PQT and P3HT respectively, (d-f) correspond to their HR-TEM images, while the film progression direction is shown through black arrows.

folding introduces constraints in the growth of crystalline domains by limiting the successive molecular chain packing as well as causes lattice parameter fluctuation, which we have observed in the interplanar spacing calculation along π-π stacking direction (using GATAN-software) for all three polymer films. It is found that chain folding is more likely in case of P3HT as compared to PBTTT because of a higher degree of backbone flexibility. Now, a thorough analysis of the individual crystalline domain for all three polymer films divulge the existence of a periodic contrast modulation with a period of 3.53±0.14 Å, 3.64±0.03 Å and 3.6±0.18 Å for PBTTT, PQT and P3HT, respectively. These contrast modulation in the BF image corresponds to the succession of electron-rich conjugated polythiophene backbones, and the intervals are congruous with the interplanar spacing, $d_{(010)}$, which means films prepared on a hydrophilic liquid substrate favor "edge-on"

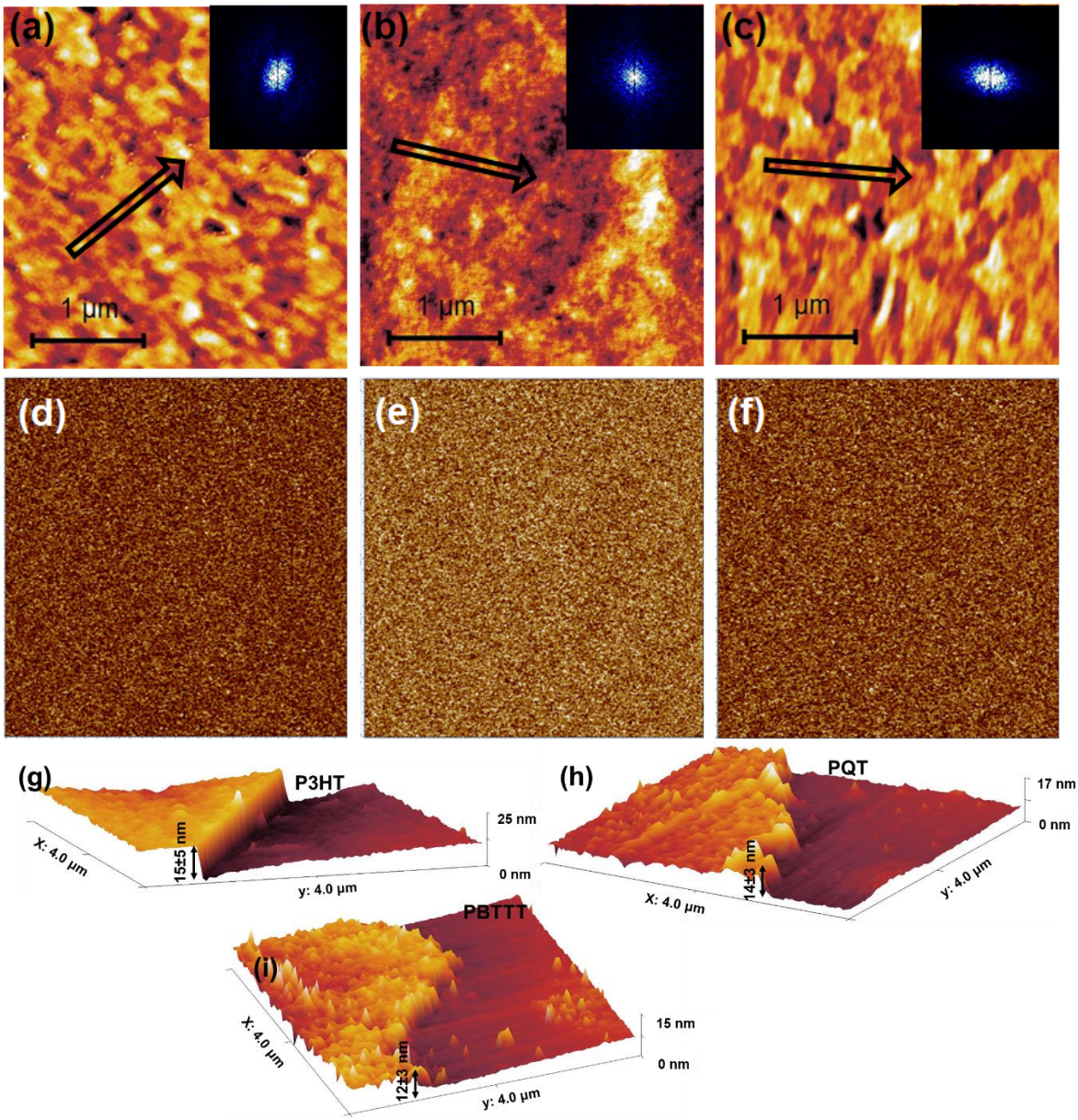

Figure 3.4 (a-c) AFM height profile of PBTTT, PQT and P3HT thin films respectively and the black arrows are indicating the FTM film progression direction as maintained during sample preparation, (d-f) represents the work function mapping, and (g-i) shows the film thickness measurements.

orientation. Thus, both XRD and HR-TEM results evidenced the presence of paracrystallinity and lattice parameter fluctuation in the FTM films along both side-chain stacking as well as π-π stacking direction.

After that, to investigate the effect of cumulative disorder and finite coherence length on the surface topography of the polymer films, atomic force microscopy [Figure 3.4 (a-c)] is

Table 3.2 Surface roughness parameters:

Samples	**Average roughness, R_a (nm)**	**R.M.S. roughness, R_{rms} (nm)**	**R.M.S. contact potential difference, V_{CPD} (mV)**
PBTTT	11.42	1.98	2.13
PQT	2.05	0.52	2.15
P3HT	12.24	2.23	2.20

being utilized at room temperature. The topographical isotropicity is clear from the 2D FFT (Fast Fourier Transform) image shown in the inset of Figure 3.4 (a-c). This is crucial for developing a better interface between the electrode and active material, facilitating easy charge generation and injection through the electrode by delocalizing the hole wavefunction at the interface [104,105]. The normalized probability density functions corresponding to surface roughness are fitted with the Gaussian function for all three PAT films, and the findings are tabulated in Table 3.2. Among the three polymers, PQT forms the smoothest film having root mean square roughness, $\boldsymbol{R_{rms}}$. = 0.524 nm while P3HT films have the highest surface roughness, $\boldsymbol{R_{rms}}$ = 2.232 nm. This is because the degree of aggregation and cluster formation is most likely in case of P3HT and PBTTT backbones as compared to PQT while developing FTM films over mobile liquid substrate, keeping all the conditions the same. While preparing the polymeric solution, we found out that the solubility of the polymers in chloroform is in the order PQT>P3HT>PBTTT. The higher aggregation probability for PBTTT is because of low-energy planar backbone conformation due to reduced steric hindrance among adjoined alkyl side-chain [48]. In case of P3HT, regio-regular grafting of only 6C-alkyl side chain is the main reason for less solubility than PQT. Thus, although we are spreading hot polymeric solutions during FTM film fabrication, having a different degree of inter-molecular wavefunction coupling and

the paracrystallinity causes these two different topographies. To investigate the presence of any processing-induced surface defects and their effect on the device performance, Kelvin probe force microscopy (KPFM) has been used at room temperature in amplitude modulation mode. Probing the electrostatic interaction between the conducting AFM tip (Pt-coated Si tip, HA_NC/Pt) and film surface, KPFM measures the local contact potential difference between them [106,107]. Thus, KPFM reconstructs the exact surface potential of the polymer films almost in real time with high spatial resolution. Figure 3.4 (d-f) shows the work function mapping of PBTTT, PQT, and P3HT films, respectively. As the top surface contain the same alkyl side-chains in an edge-on dominated structure, so almost similar contact potential difference, V_{CPD} for all three PAT films is justified.

In order to get a macroscopic perspective of the electronic band structure of solid polymeric films, we have used UV-vis absorption spectroscopy at room temperature (Figure 3.5 (a)). The 2D electronic dispersion due to intrachain π-conjugation and intermolecular coupling among the proximate monomer motifs contributes to these well-structured absorption spectra. Among the first two absorption peaks, the low energy vibronic shoulder, located at ~600 nm for PBTTT and ~589 nm for P3HT and PQT, respectively, is attributed to the 0-0 transition [108]. The bathochromic spectral shift in the case of PBTTT film is mainly because of the higher resonance stabilization energy of linearly symmetrical thieno[3,2-b]thiophene restricts the delocalization of electron clouds to single thiophene units and thus brings the HOMO (highest occupied molecular orbital) as well as LUMO (lowest unoccupied molecular orbital) to a lower energy level. Now, to evaluate the optical band-gap, i.e., energy corresponding to the lowest electronic transition by photon absorption, we have used the Tauc relation, [109]

$$\alpha\hbar\omega = C\left(\hbar\omega - E_g\right)^m \tag{3.3}$$

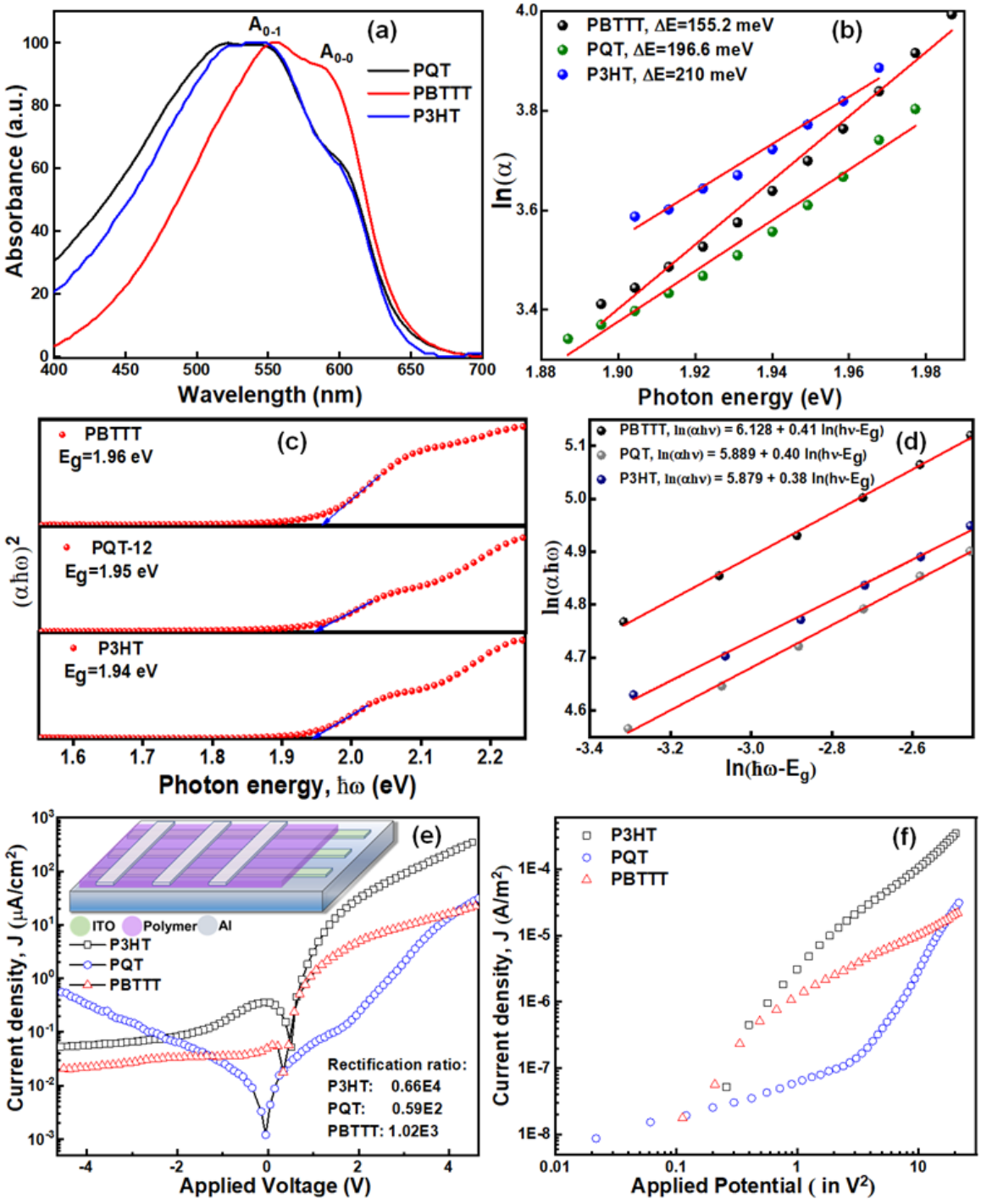

Figure 3.5 (a) Electronic absorption spectra, (b) corresponding low-energy absorption line-shape analysis, (c) optical band gap, and (d) order-of-transition plot for self-assembled P3HT, PQT and PBTTT thin films measured over a glass substrate. Current density vs voltage characteristics [(e) J-V, (f) J-V^2] of the Schottky barrier diodes (SBDs) along with the device schematic in the inset.

where C is a proportionality constant, α represents the absorption co-efficient, $\hbar\omega$ is the photon energy and m stands for the order of transition. Considering the transition for all

three polymers a direct-allowed type for which $m = {}^{1}/_{2}$, we have calculated the optical band-gap from the $(\alpha\hbar\omega)^2\ vs\ \hbar\omega$ plot (Figure 3.5 (c)). In thin-film form, we found the optical band-gaps are almost similar, 1.94 eV, 1.95 eV and 1.96 eV for P3HT, PQT and PBTTT respectively. Hence, to prove our previous assumption of direct-allowed type 0-0 transition, we tried both the direct and indirect type transition plot and got the better linearity in case of direct-allowed type transition [109]. Then, we rearranged the Tauc relation as, $ln(\alpha\hbar\omega) = lnC + m\ ln(\hbar\omega - E_g)$, and from the slope of $ln(\alpha\hbar\omega)\ vs\ ln(\hbar\omega - E_g)$ plot, we got the 'm' values close to 0.5 and thus justifying the direct type band-gap in all three polymers (Figure 3.5 (d)).

Now, as evidenced from the XRD and HR-TEM results, the presence of paracrystallinity and other static disorders can cause the exponential tailing of the absorption band edge by introducing microscopic perturbations [92,110]. Thus, we can get insight into the exciton-phonon interaction and their coupling strength by analyzing the absorption line shape in this lowest energy 0-0 transition region. The absorption line shape at low energy region usually is analyzed by using the well-known Urbach rule, [111,112]

$$\alpha = \alpha_0\ exp[-\sigma_T(\hbar\omega_0 - \hbar\omega)/K_BT] \tag{3.4}$$

where α_0 represents the absorption co-efficient at a converging energy $\hbar\omega_0$, σ_T is the steepness constant, and K_B stands for Boltzmann constant. Thus, from the $\ln(\alpha)\ vs\ \hbar\omega$ plot [Figure 3.5 (b)], we got the value of Urbach energy, E_U $(= K_BT/\sigma_T)$ which is lowest for PBTTT, 155.2 meV and highest for P3HT, 210 meV. This is because the rotational invariance of fused aromatic rings in the PBTTT backbone facilitates the formation of highly ordered in-plane π-stacking by adopting a more planar backbone conformation compared to the highly flexible P3HT and also PQT backbones. As the 2-dimensional *bc*-plane is richer with electron density than the *a*-direction, and the well-separated alkyl

chains (>5Å) make the excitonic interactions less probable, Urbach tailing arises mainly from the in-plane π-π stacking disorder mediated exciton scattering. This microcrystalline disorder localizes the density of states and thus the steepness parameter, σ_T anticipated being temperature invariant. But Luisa et al. and Kenichi et al. [110,112] found that σ_T elevates initially with temperature and then it saturates to a limiting value σ_0 after 40-200 K depending upon the type of material. In our case, as we have measured all the absorption spectra at 300 K, thus steepness parameter calculated from Urbach slope ($= \sigma_T {K_B}^{-1} T^{-1}$) should be the asymptotic limiting value σ_0. According to Toyozawa et.al., the reciprocal of this limiting steepness parameter is approximately proportional to the strength of the exciton-phonon coupling, ${\sigma_0}^{-1} = \xi \chi^{-1}$, where χ is a dimensionality constant (χ = 1.24 and 1.5 for 2-D and 3-D systems respectively) and ξ stands for the exciton-phonon coupling constant. For our case, considering 2-D case (as bc-plane dominating), the value of ξ are found to be 7.44, 9.43 and 10.07 for PBTTT, PQT and P3HT respectively. Thus, excitons are strongly coupled with the phonon fields in all three polymers (as $\xi > 1$), which will momentarily give birth to trap states [93,111–113].

3.2.3. Charge transport study

Finally, to study the compound effect of intragrain paracrystallinity and structural coherence length on the out-of-plane and in-plane charge transport, we have used the conventional SBD (Al/PAT/ITO) and FET (Si/SiO_2/PAT/Au) structure. Unlike p-n junction diodes, a unipolar conduction mechanism applies to the SBD structure as current is controlled by the majority carrier (hole in case of PAT) only. Thus, a high Schottky barrier leads to large rectification ratio (RR) by effectively blocking the current flow in reverse bias. As the HOMO levels are 4.92eV, 5.03eV and 5.06 eV for P3HT, PQT and PBTTT, respectively, we have chosen ITO (4.9eV) and Al (4.08eV) for ohmic and Schottky

junction formation. Now, the gaussian-like distribution of hole wavefunction in the HOMO level usually having a tail on higher energy side allows the thermionic emission of holes from the semiconductor side to metal side after junction formation to equilibrate the Fermi level. Thus, the asymmetric J-V characteristics, as shown in Figure 3.5 (e), can be explained by the thermionic emission model and Mott-Gurney law related to the space charge limited current (SCLC). Thermionic emission-diffusion theory relates current density with the applied bias voltage as [81,114]:

$$J = J_0\left[exp\left(\frac{qV}{\eta K_B T}\right) - 1\right] \qquad \text{and} \qquad J_0 = A^* T^2 exp\left(-\frac{q\varphi_B}{K_B T}\right) \tag{3.5}$$

where reverse saturation current density, J_0 and ideality factor, η normally determined from the intercept and slope of the linear region in J-V plot. After that, to calculate the Schottky barrier height, φ_B which governs the RR of SBDs, we have taken the value of Richardson constant, A^*= 2×10^{-9}A cm^{-2} K^{-2} which was experimentally evaluated from the typical Richardson plot in case of P3HT by the Kaneto and Takashima [115]. However, after filling all the bulk and interfacial traps at high forward bias, the current flow becomes limited by the injected holes only. Thus, the intrinsic hole mobility (μ_h) along the out-of-plane direction in 200nm (= d) thick PAT films has been determined from the J-V^2 plot [Figure 3.5 (f)] using the standard Mott-Gurney relation:

$$J = \frac{9\epsilon\mu_h}{8}\left(\frac{V^2}{d^3}\right) \tag{3.6}$$

All the calculated parameters are tabulated in Table 3.3 while the used symbols reflect the common physical parameters [31]. The Schottky barrier height is found to be highest for P3HT, validating the highest RR value (0.66×10^4) among all the polymers, while PQT shows the lowest RR as well as the lowest φ_B and μ_h. But it is contradicting to our XRD

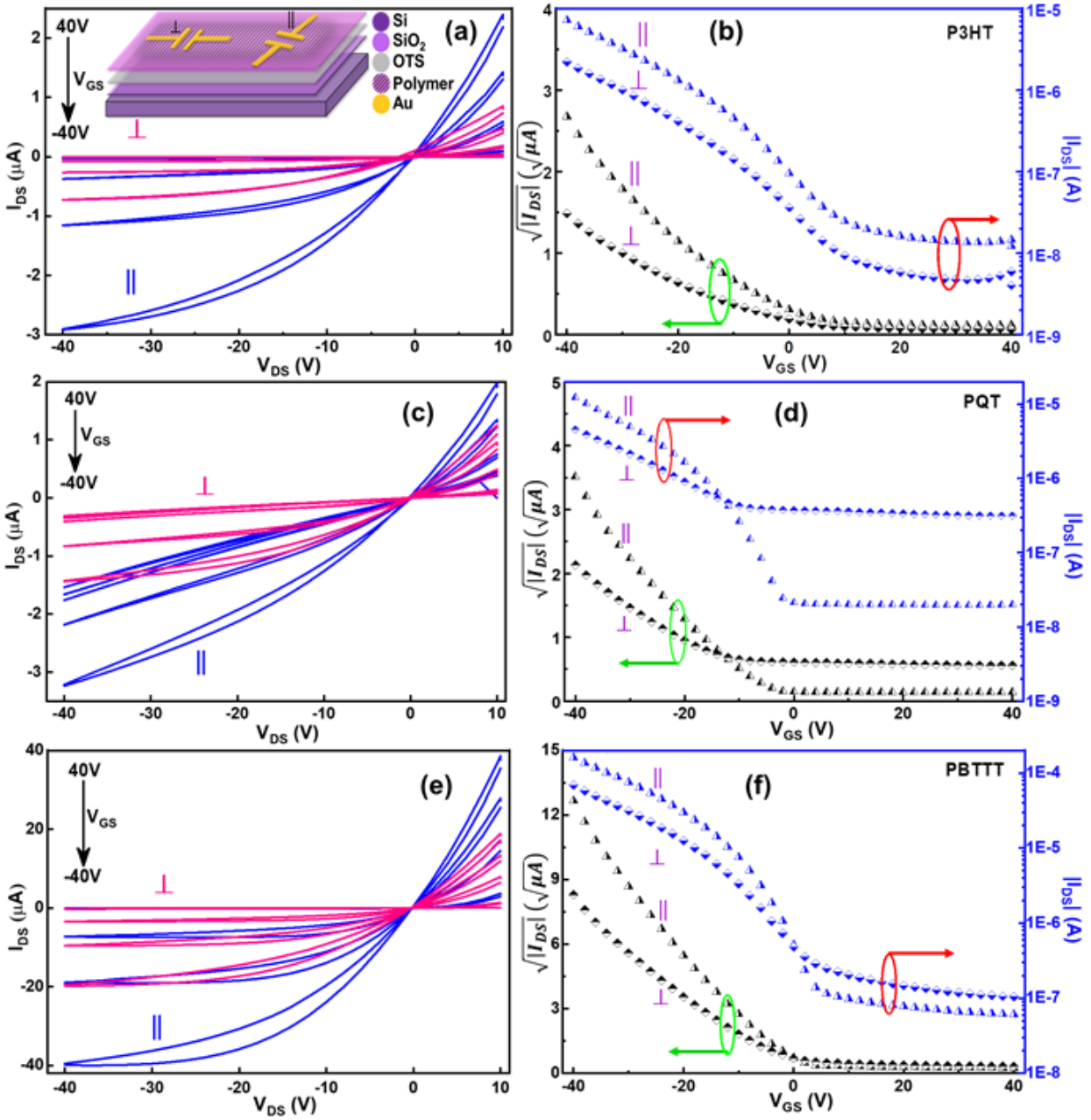

Figure 3.6 Output and transfer characteristics of P3HT (a,b), PQT (c,d) and PBTTT (e,f) OFETs along with the schematic representation in the inset of (a).

findings of lowest intragrain paracrystallinity and lattice parameter fluctuation in case of PQT if we consider, charge transport is fully dominated by the trapping and scattering from defect states. This inconsistency can be explained as, interfacial traps cause an increase in contact resistance (R_C) while the bulk resistance (R_B) is inversely proportional to the film crystallinity. Moreover, large structural coherence length for P3HT and PBTTT accounts

for higher μ_h by reducing effective grain boundary resistance towards carrier mobility. The lower alkyl chain length also provides lesser resistance in P3HT, leading to the highest out-of-plane hole mobility in the case of edge-on stacking. Now, to investigate the in-plane hole mobility, we have fabricated organic field effect transistors (OFET) with channels parallel and perpendicular to the polymer backbone orientation. The comparative output and transfer characteristics are shown in Figure 3.6, while all other electrical parameters have been evaluated from the saturation region using the following relations,

$$I_{DS} = \mu C \frac{W}{2L}(V_{GS} - V_{Th})^2 \tag{3.7}$$

$$SS = \left[\frac{d(logI_{DS})}{dV_{GS}}\right]^{-1} \tag{3.8}$$

$$N_{SS}^{max} = \left[\frac{SS \times \log e}{K_B T/q}\right]\frac{C}{q} \tag{3.9}$$

where I_{DS}, SS, N_{SS}^{max}, V_{GS}, V_{Th}, and C represents saturation drain current, subthreshold swing, trap density, gate voltage, threshold voltage and capacitance of SiO_2 per unit area, respectively.[75,116] Both types of OFETs (∥ and ⊥) were made on the same substrate (Si/SiO_2), having the same roughness with channel width (W) and length (L) 2mm and 20μm, respectively. Thus, the findings of in- plane measurement can be attributed to the effect of polymeric backbone assembly configuration, structural defects, charge carrier-phonon coupling strength and delocalization of hole wavefunction only. In an edge-on dominated configuration, μ_h along the polymer backbone (∥) as-well-as π-stacking (⊥) direction found to be highest in case of PBTTT and lowest for P3HT. Since higher active material roughness causes carrier scattering in the OFET channel, dielectric/PAT interfacial trap density should be in the following order P3HT>PBTTT>PQT (as found in AFM). In case of inorganic semiconductors, interfacial trap density usually governs the

mobility, but for organic molecules, the carrier flowing path is also very important. For PBTTT, the fused aromatic ring-induced backbone rigidity facilitates the planar

Table 3.3 Electrical parameters of thin solid FTM films made of three polythiophene derivatives.

Out-of-plane SBD measurement	**Hole mobility ($cm^2 V^{-1} s^{-1}$)**	**Reverse saturation current density ($nA\ cm^{-2}$)**	**Barrier height (meV)**	**Ideality factor**
P3HT	3.7×10^{-5}	41.79	216.4	4.10
PQT	0.7×10^{-5}	83.70	198.4	6.13
PBTTT	2.7×10^{-5}	50.42	211.5	4.29
In-plane Transistor measurement	**Hole mobility ($cm^2 V^{-1} s^{-1}$)**	**Threshold voltage (V)**	**Subthreshold swing (V/dec)**	**Trap density (cm^{-2})**
P3HT				
Parallel	11.2×10^{-3}	5.99	15.0	1.57×10^{13}
Perpendicular	3.25×10^{-3}	5.05	16.9	1.77×10^{13}
PQT				
Parallel	21.0×10^{-3}	7.94	7.97	0.84×10^{13}
Perpendicular	8.89×10^{-3}	5.54	27.8	2.92×10^{13}
PBTTT				
Parallel	234×10^{-3}	4.48	7.1	0.74×10^{13}
Perpendicular	96.5×10^{-3}	4.35	12.8	1.35×10^{13}

conformation and thus helps to create a low resistive path for charge carriers to flow, overcoming the interface effect. The overall trap density calculated from the subthreshold swing is also lowest along the PBTTT backbone direction.

Therefore, while the transistor is working on accumulation mode, after filling all the interfacial traps, how fast the accumulated holes will move with respect to the applied electric field will solely depend on the polymeric backbone assembly configuration. Thus, the careful design of backbone structure providing more rigidity and proper side-chain

density should further improve the in-plane mobility, while by limiting the side-chain length (optimizing the solubility), out-of-plane mobility can further be enhanced. Apart from molecular engineering, to develop a high-performing electronic device (diode and transistor) using organic semiconducting materials with less parasitic current, we need to manipulate the origin of edge-on formation and associated defects while preparing the active material. In this regard, with the help of our proposed model mechanism, one can tune the polymeric self-assembly at air-liquid interface by simply changing the Marangoni flow, viscous force, evaporation rate and surface tension gradient.

3.3.Conclusions

In conclusion, we have successfully demonstrated a model to elucidate the spreading of polymeric solution on a high surface-energy liquid substrate and thin-film growth mechanism by considering all possible flow processes. The paracrystalline disorder and lattice parameter fluctuation associated with this complex flow process have been quantified along the a-axis and found to be highest for the flexible P3HT backbone and 14-C PBTTT backbone. After that, the local in-plane orientation along with lattice bending and fluctuation in interlamellar spacing has also been directly probed at nanometer-level through HR-TEM images. The evolution of surface topography studied using AFM and work function mapping reflects these three polymers' solubility-led aggregation probability. Moreover, the Urbach tail width quantification and corresponding exciton-phonon coupling strength evidenced that PBTTT is the least affected backbone while P3HT is the most affected one due to these microstructural perturbations. Finally, the highest out-of-plane hole mobility is found for P3HT, while PBTTT shows maximum mobility along in-plane (both $\parallel$ and $\perp$) in our particular processing condition. The measurement of charge carrier transport properties along all three directions helps us establish the proper

understanding of structure-property correlation. Self-assembly at air-liquid interface also provides electrically highly anisotropic active material, while the anisotropicity and mobility can be improved drastically by further optimizing the processing conditions. Thus, we can design high-performing electronic devices according to our needs through proper backbone engineering and then by simply manipulating the forces acting at the air-liquid interface during polymer film formation.